Correspondence to:
D. C. A. Lima,
dclima@fc.ul.pt

How Will a Warming Climate Affect the Benguela Coastal Low-Level Wind Jet?

Daniela C. A. Lima[1] [iD], Pedro M. M. Soares[1] [iD], Alvaro Semedo[2,1] [iD], Rita M. Cardoso[1] [iD], William Cabos[3] [iD], and Dmitry V. Sein[4,5] [iD]

[1]Instituto Dom Luiz, Faculdade de Ciências, Universidade de Lisboa, Lisboa, Portugal, [2]Department of Water Science and Engineering, IHE Delft, Delft, The Netherlands, [3]Department of Physics and Mathematics, University of Alcalá, Madrid, Spain, [4]Alfred Wegener Institute for Polar and Marine Research, Bremerhaven, Germany, [5]Shirshov Institute of Oceanology, Russian Academy of Science, Moscow, Russia

Abstract The strong coastal upwelling associated to the Benguela eastern boundary upwelling system makes the ocean along coast of this current one of the most productive ecosystems in the world. The Benguela Coastal Low-Level Jet (BCLLJ) is one of the most important mesoscale feature that shape the climate of this region. The main synoptic forcing of the BCLLJ is the Angola thermal low over land and the St. Helen anticyclone over the ocean, resulting in southwesterly winds along the coast. This study investigates how the BCLLJ might change due to climate warming, with the help of uncoupled and coupled simulations from a 25-km horizontal resolution regional climate model (ROM). In general, the coupled simulation displays the best performance in representing the present time near-surface wind speed, with a decrease on the known warm bias of sea surface temperature in the Benguela eastern boundary upwelling system region. The analysis of the projected changes of the BCLLJ climate toward the end of the 21st century (2070–2099), following the RCP8.5 emissions scenario, shows an increase in the frequency of the BCLLJ occurrence along the southern area with higher changes in the coupled simulation (between 6% and 8%). These changes are related to a southerly shift of the St. Helen High, which intensifies the flow offshore the west coast of South Africa and causes a sharpening of the land-sea thermal contrasts. However, during spring, associated with the decrease in near-surface wind speed due to higher sea surface temperatures, the future frequency and intensity of the BCLLJ are lower.

1. Introduction

It is expected that during the 21st century the climate will continue to warm, essentially due to the enhancement of greenhouse gases concentration in the atmosphere (Intergovernmental Panel on Climate Change, 2014). This global warming is associated to several impacts in all regions of the world, particularly in the eastern boundary upwelling system (EBUS) areas, which are considered to be among the most vulnerable spots to climate change (Bakun et al., 2015; Sydeman et al., 2014; D. Wang et al., 2015). In the EBUS regions, the feedbacks between atmosphere, land, and ocean play a crucial role in defining the respective regional climates. Here upwelling, coastal low-level jets (CLLJs), and marine boundary layer clouds are some of the physical processes that influence coastal weather. Along the EBUSs, the sea surface temperature (SST) decreases due to upwelling, which leads to a reduction of the evaporation over the ocean and subsequently to less water vapor content in the marine atmospheric boundary layer (MABL). Over land, the water vapor content in the air is even lower, due to the strong coastal-parallel winds in the EBUSs, which inhibit the advection of marine air inshore. Coastal jets are usually found along the equatorward eastern boundary currents (California, Canary, Humboldt, Benguela, and West Australia), due to a large-scale synoptic forcing (Lima et al., 2018; Ranjha et al., 2013; Winant et al., 1988). However, CLLJs can also be found along the southeast Arabian Peninsula (Ranjha et al., 2015) and over the Bohai Sea and Yellow Sea (D. Li et al., 2018). The synoptic forcing of the eastern boundary currents CLLJs is characterized by semipermanent high-pressure systems over the ocean and the thermal low over land, resulting in strong coastal parallel winds.

Upwelling events in the EBUS bring rich in nutrients cold water from the deep ocean to the surface, making them important habitats for marine biodiversity (Fréon et al., 2009). Therefore, although they represent only 2% of the global ocean surface, the EBUSs are among the most productive ocean ecosystems and have a

strong economic impact through increased fish stocks. The contribution of these regions to the global marine fisheries is higher than 20%. The evolution of these important upwelling systems in climate change projections (e.g., Bakun et al., 2015; Wang et al., 2015), as well as the impacts of climate change on CLLJs (Cardoso et al., 2016; Semedo et al., 2016; Soares et al., 2017; Soares et al., 2018), has been studied by different authors. Wang et al. (2015) showed the expected changes in terms of timing, duration, and intensity of the upwelling events in the EBUS. In this study, the authors revealed an expansion of the upwelling season, starting earlier and ending later. Three out of four EBUSs (Canary, Humboldt, and Benguela) displayed a consistent increase in the duration and intensity of upwelling events at higher latitudes. Recently, Semedo et al. (2016) presented the first future global projections of the CLLJs using an ensemble of two EC-Earth global climate model simulations. This study projected a significant increase in the frequency of CLLJ occurrences toward the end of 21st century mostly in Iberia and Oman. In the case of the Benguela CLLJ a projected increase of the frequency of occurrence around 26°S and a decrease around 17.5°S was expected. The global projections of the CLLJ frequency of occurrence are shown to have a consistent relationship with the upwelling ones. These projections are consistent with the expected changes of upwelling, which may lead to a reinforcement of the positive feedback between both phenomena, playing a decisive role in the future of the regional climate. In California, neither the upwelling events nor the occurrence of the coastal jet are projected to significantly change under warming climate (Semedo et al., 2016; D. Wang et al., 2015). The latter studies revealed the need to deepen the assessment of the impact of climate change signal on the CLLJ regions, such as the Benguela CLLJ (BCLLJ).

Recently, (Lima et al., 2019) presented a detailed climatology of the BCLLJ for present climate (1980–2014), at high resolution. Using ERA-Interim reanalysis as lateral boundary conditions, the temporal and spatial variability, dynamics, and vertical structure of BCLLJ were investigated with the help of the regional model ROM (REMO-OASIS-MPIOM), in uncoupled mode at 25-km horizontal resolution (Sein et al., 2015). The semipermanent St. Helen high-pressure system over the South Atlantic Ocean and the inland Angola and Kalahari thermal low-pressure systems represent the synoptic forcing behind the BCLLJ. The BCLLJ is an important mesoscale feature in Namibia and Angola coastal areas. The extreme aridity of the Namib Desert may be enhanced due to the BCLLJ occurrence (Nicholson, 2010). The BCLLJ is present all year round with a marked seasonal cycle (Lima et al., 2018, 2019). It is characterized by two local maxima of frequency of occurrence, at 17.5°S (northern area) and at 26°S (southern area). During the austral summer, the BCLLJ is located in a more southern area with a persistency of about 60%. The coastal jet becomes less frequent and migrates equatorward during the austral autumn and winter. During the austral spring, the BCLLJ is found in northern area and has a frequency of occurrence of around 45%. The seasonality of the BCLLJ shows a strong link with the seasonal cycle of the zonal and meridional components of the momentum budget (Lima et al., 2019). The BCLLJ is characterized by a wind speed maximum above 20 m/s that occur around 400–500 m above sea level (a.s.l.), within or at the top of the MABL temperature inversion (Beardsley et al., 1987; Lima et al., 2018, 2019; Ranjha et al., 2013). The strong subsidence of warm air from the St. Helen high-pressure system over the MABL, in contact with cold air near the ocean surface, generates a strong capping temperature inversion (Lima et al., 2019). The temperature of the MABL decreases toward the coast due to low SST, which results in a sloping inversion. This sloping inversion implies a horizontal temperature gradient, which is related to a thermal circulation (Parish, 2000), separating the ocean cooler air from continental warm air. From the sloping inversion, a thermal wind structure develops, which leads to an increasing in the wind speed with the decreasing height. However, within the MABL, the surface friction slows down the air flow closer to the surface, which generates a jet-shaped vertical wind speed profile, with a maximum wind speed below or at the capping inversion (Beardsley et al., 1987; Zemba & Friehe, 1987). Below the temperature inversion, the air is well mixed resulting from the turbulent flow due to the vertical wind shear. Therefore, the thermal wind has the same direction of the synoptic flow caused by the strong horizontal temperature gradient. Above the inversion, the atmospheric layer is stable, and the wind shear is owing to the baroclinicity, resulting in an opposite direction of the thermal wind. The intensity of the BCLLJ has a seasonal cycle associated with the subsiding air. At 17.82°S, the mean jet wind speed is highest in spring and at 16.4°S is during summer season (Lima et al., 2019).

The present study investigates the signal of the climate change on the BCLLJ toward the end of the 21st century. The main goal is to understand how the BCLLJ frequency of occurrence and its main properties might change in a warming climate context. This paper uses four regional climate ROM simulations in uncoupled

and coupled modes for two periods: historical (1976–2005) and future (2070–2099), following the RCP8.5 greenhouse gases emissions scenario (Riahi et al., 2011) in the latter. All the regional climate simulations use a 25-km horizontal resolution and are forced by the global climate model (GCM) Max-Planck Institute Earth System Model (MPI-ESM; Giorgetta et al., 2013) as lateral boundary conditions. The current investigation is focused on the projected changes of the Benguela CLLJ toward the end of the 21st century, concerning its temporal and spatial variability and future mean properties. A characterization of the seasonal and annual cycle of BCLLJ frequency of occurrence and its main properties of the jet, like jet intensity, is presented. The projected changes of the BCLLJ synoptic forcing and land-sea thermal contrast are also analyzed. The analysis of the future projections of the near-surface wind speed is supported with a multimodel ensemble of the regional climate simulations under the framework of the CORDEX-Africa effort (Giorgi et al., 2009).

The current manuscript is structured as follows. In section 2, the regional climate simulations and the methodology are described. The evaluation of the regional climate models used are presented in section 3, and in section 4, the impact of the climate change on the BCLLJ is discussed. Finally, in section 5 the main conclusions of this study are presented.

2. Data and Methodology

2.1. ROM Simulations

To assess the impact of climate change on the BCLLJ, a set of regional climate simulations are used. Four ROM (REMO-OASIS-MPIOM) simulations in stand-alone atmosphere mode and in atmosphere-ocean coupled mode (Sein et al., 2015), forced by MPI-ESM, are used for both historical and future climates. The regionally coupled model comprises the Regional Atmospheric Model (REMO; Jacob et al., 2001) coupled to a global oceanic model, the Max Planck Institute Ocean Model (MPIOM), that includes modules of sea ice and marine biogeochemistry. These models are coupled through the OASIS coupler, which is configured with a coupling period of 3-hr model time. The atmospheric component of MPI-ESM is used to force MPIOM outside of the region of coupling (that coincides with the REMO domain), and for the REMO lateral boundary conditions in both uncoupled and coupled simulations.

In the present study, the historical climate simulations cover the period from 1976 to 2005, and 2070–2099 is considered for the future climate runs, according to the RCP8.5 greenhouse gas emissions scenario. These runs have a 25-km horizontal resolution with 31 hybrid vertical levels and a 3-hourly temporal resolution. The atmospheric domain of the simulations covers the African continent, a large part of Atlantic Ocean, the Mediterranean region, and parts of the Indian Ocean (Figure 1a). The MPIOM configuration has the grid pole over the Northeastern Africa, and the horizontal resolution reaches 7–25 km near the West African coasts and 60–65 km in equatorial Atlantic (Figure 1b).

2.2. CORDEX-Africa Simulations

A set of Africa regional climate simulations from the Coordinated Regional Climate Downscaling experiment (CORDEX; Giorgi et al., 2009) are also used, to support and understand the relative performance of the ROM simulations. Since the model levels of the CORDEX-Africa data set are not available for download, only the near-surface data are used in this study. The daily mean wind speed at 10-m height from 19 CORDEX-Africa simulations at 0.44° horizontal resolution was considered for the historical period (1976–2005) and for the RCP8.5 future emission scenarios (2070–2099). The CORDEX-Africa simulations and the GCM forcing used by each institution are presented in Table 1, with a different institution acronym assigned.

2.3. Observations

The 10-m wind speed from the ROM and CORDEX-Africa RCMs simulations are evaluated by comparison against the Cross-Calibrated Multi-Platform (CCMP) data set (Atlas et al., 2011). The SST results of ROM simulations are evaluated against the National Oceanic and Atmospheric Administration (NOAA) SST fields (Reynolds et al., 2007). CCMP is a wind product built by the National Aeronautics and Space Administration, with a horizontal resolution of 0.258° and a 6-hourly output, covering the period from July 1987 to June 2011. The cross-calibrated multiple satellite data sets were combined with in situ observations, remote sensing, and European Centre for Medium-Range Weather Forecasts reanalysis, through a
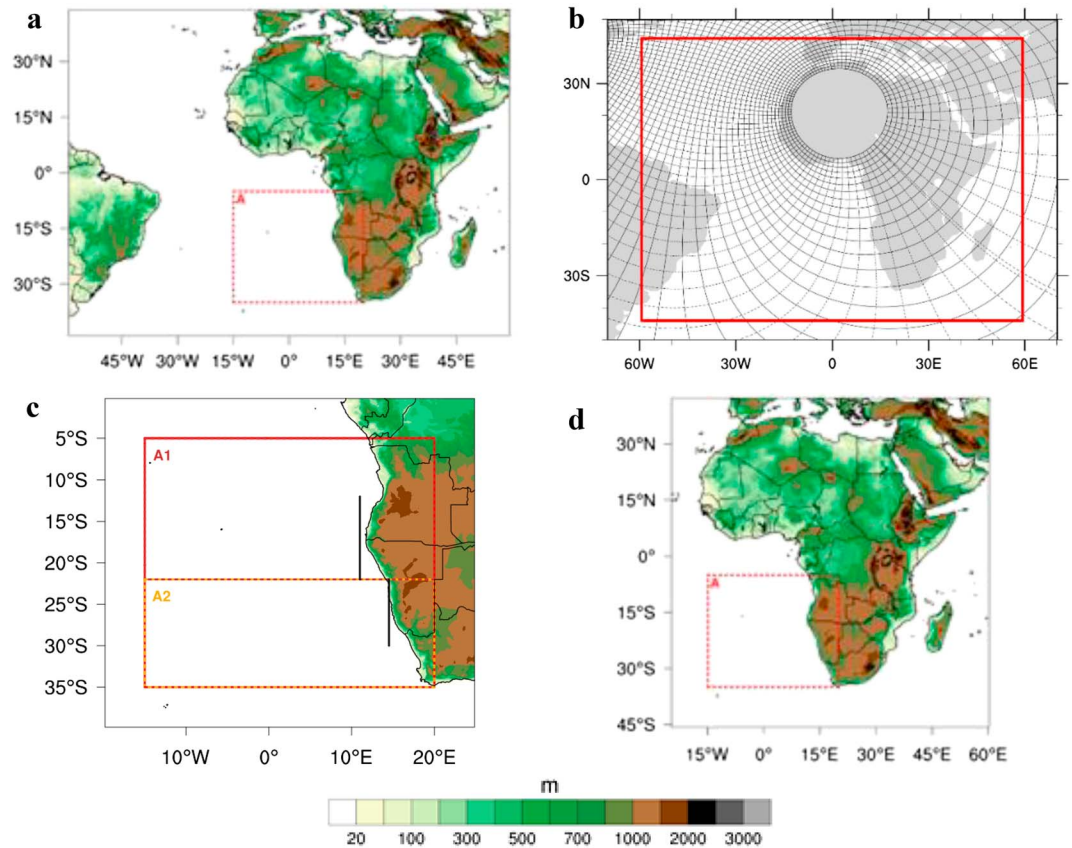
Figure 1. (a) ROM Model domain, (b) ROM ocean horizontal grid, (c) a zoom in interest area (A) in a, and (d) the CORDEX-Africa domain. Dash red line delimits the area A of analysis regarding the BCLLJ. Dash brown and orange lines delimit the subareas A1 and A2, respectively. The contours represent the model topography. The solid black lines mark the two representative along sections.

variational analysis method. The NOAA Optimum Interpolation Sea Surface Temperature V2 high-resolution data set combines ocean temperature derived from satellite and in situ measurements and model analysis (Reynolds et al., 2007). The daily SST fields have a $0.25° \times 0.25°$ spatial resolution and span from September 1981 to the present time.

2.4. RCMs evaluation

To perform the assessment of the climate change impact on the BCLLJ, the evaluation of the simulations historical period is an important first step. Since the historical simulations (1976–2005) use global climate models as lateral boundary conditions, they have a daily nonsynchronized climate when compared with the observations. Consequently, only a statistical comparison can be performed between the ROMs or the CORDEX-Africa runs and the observations. Therefore, a Julian year with 366 daily means was computed for each RCM and observational data set. Thus, the use of this daily climatology makes possible the comparison between the observations and the nonsynchronized present climate simulated by the ROM and CORDEX-Africa simulations.

The near-surface wind speed from ROM and CORDEX-Africa runs were compared against the CCMP data set. As the models and the CCMP have different horizontal resolutions, the fields with higher resolution were interpolated to the grid with coarser resolution. In the case of the uncoupled and coupled ROM simulations, simulated 10-m winds were interpolated to the CCMP grid at $0.25°$ using the nearest-neighbor point on the grid. Conversely, the CCMP was interpolated for the CORDEX-Africa regular nonrotated grid at $0.44°$ using the same interpolation method. Also, the SST fields from ROM are compared against the NOAA SST data set and were interpolated conservatively to the NOAA's grid. As in Lima et al. (2019), the error metrics

Table 1
CORDEX-Africa RCMs used in the Current Study, Along with the Respective Forcing GCM, and the Respective Acronym

Global Climate Model (forcing models)	CORDEX-Africa Regional Climate Model	Acronym	Institution	Reference
ICHEC-EC-EARTH	CCLM4-8-17	CLM1	Climate-limited area Modeling Community	Rockel et al. (2008)
MOHC-HadGEM2-ES		CLM2		
CNRM-CERFACS-CNRM-CM5		CLM3		
MPI-M-MPI-ESM-LR		CLM4		
ICHEC-EC-EARTH	HIRHAM5	DMI	Danish Meteorological Institute	Christensen et al. (2007)
ICHEC-EC-EARTH	RACMO22E	KNMI1	Koninklijk Nederlands	Van Meijgaard et al. (2008)
MOHC-HadGEM2-ES		KNMI2	Meteorologisch Instituut	
ICHEC-EC-EARTH	REMO2009	MPI1	Helmholtz-Zentrum Geesthacht, Climate Service Center, Max Planck Institute for Meteorology	Jacob et al. (2001)
MPI-M-MPI-ESM-LR		MPI2		
ICHEC-EC-EARTH	RCA4	SMHI1	Swedish Meteorological and Hydrological Institute	Samuelsson et al. (2011)
MOHC-HadGEM2-ES		SMHI2		
CNRM-CERFACS-CNRM-CM5		SMHI3		
MPI-M-MPI-ESM-LR		SMHI4		
IPSL-IPSL-CM5A-MR		SMHI5		
CCCma-CanESM2		SMHI6		
CSIRO-QCCCE-CSIRO-Mk3-6-0		SMHI7		
MIROC-MIROC5		SMHI8		
NCC-NorESM1-M		SMHI9		
NOAA-GFDL-GFDL-ESM2M		SMHI10		

are computed for each grid point and time scale (monthly, seasonal, and yearly): bias, bias%, mean absolute error (MAE), mean absolute percentage error (MAPE), root-mean-square error (RMSE), normalized standard deviation, spatial correlation (Wilks, 2006), and Willmott-D score (Willmott et al., 2012). The Willmott-D score, which measures the differences in the mean and standard deviation, has a perfect skill when $D = 1$ and no skill when $D = -1$. The probability density function (PDF) matching scores (Perkins et al., 2007) and Yule-Kendall skewness measure (Ferro et al., 2005) are also computed to measure the differences between the distributions. The difference between the observed and modeled PDF skewness is evaluated with the Yule-Kendall skewness measure.

A multimodel ensemble of the CORDEX-Africa RCMs (EnsFull) was built, to perform a more robust evaluation of the near-surface wind speed response to global warming (J. H. Christensen et al., 2010). This ensemble mean is based on the relative performance of each CORDEX-Africa RCM (Cardoso et al., 2018; Soares et al., 2017). The bias% and MAPE are not included in the ensemble building. For bias, MAE, and RMSE, the inverse of its absolute value is first computed, since the optimal result is zero. As the best result of normalized standard deviation is 1, this metric was transformed as

$$\vartheta_n = \begin{cases} \sigma_n \ if \ \sigma_n < 1 \\ \dfrac{1}{\sigma_n} if \ \sigma_n > 1 \end{cases} \tag{1}$$

Following the same process, the Yule-Kendall became

$$YK_{new} = \begin{cases} YK + 1 \ if \ YK < 0 \\ \dfrac{1}{YK + 1} if \ YK > 0 \end{cases} \tag{2}$$

The individual model ranks, for each metric, were obtained by dividing each value by the sum of all model values, which leads to the sum of the ranks to be equal to 1. The weights of each model were constructed by

multiplying the ranks of all the metrics and then dividing by the sum of the weights. The ensemble near-surface wind speed was obtained by multiplying for respective CORDEX-Africa RCM weight as

$$\overline{\text{sfcWind}} = \frac{\sum_{i=1}^{N}\text{sfcWind}_i w_i}{\sum_{i=1}^{N} w_i} \tag{3}$$

where sfcWind$_i$ is the near-surface wind speed, w_i is the weight of each RCM, and N is the number of models. The PDF of the multimodel CORDEX-Africa ensemble was obtained as

$$\text{PDF}(\text{sfcWind}) = \sum_{i=1}^{N} \text{PDF}(\text{sfcWind})_i w_i \tag{4}$$

2.5. CLLJ Analysis

The detection algorithm of the CLLJ built by Ranjha et al. (2013) and later revised by Lima et al. (2018) is applied to the 3-hourly model output from uncoupled and coupled ROM simulations. The suggested algorithm detects a CLLJ occurrence when the jet maximum is located within the first 1,000 m above sea level and within or at the top the MABL temperature inversion. The historical (1976–2005) and future (2070–2099) wind speed and temperature vertical profiles are analyzed to identify the occurrence of a coastal jet and assess the projected future changes on the BCLLJ properties. The projected changes of the spatial and temporal variability of the BCLLJ frequency of occurrence, as well as its main properties, are investigated, following the RCP8.5 scenario. The expected changes of the synoptic forcing of the BCLLJ and of the land-ocean temperature gradients are also studied. Furthermore, the impact of the climate change on the wind speed at 10-m height is analyzed with ROM and the multimodel ensemble of CORDEX-Africa simulations.

3. Present Climate: Evaluation of Historical Simulations

The evaluation of the wind speed results at 10-m height was performed for the ROM uncoupled and coupled historical runs, for the CORDEX-Africa RCMs, and for the multimodel ensemble historical simulations, by comparison against the CCMP data set, for area A (Figure 1a). Table 2 displays the seasonal mean bias%, the MAPE, the normalized standard deviation, Willmott-D, the yearly spatial correlation, and the daily Skill (S) and Yule-Kendall skill scores. In general, the RCM results present a good description of the wind speed at 10-m height, although displaying a significant discrepancy of values, particularly the bias% and MAPE. The bias% values show a general overestimation of the near-surface wind speed for all RCMs, except for KNMI1 and SMHI7, which reveal rather small negative bias values. The MAPE values are mostly in the range of 5% to 13%, with the DMI run presenting the highest error (~18%). Regarding the seasonal normalized standard deviation, all models (except SMHI8) show values greater than 1, which reveals an overestimation of the near-surface wind speed variability. The Willmott-D score has a wide range of values, spanning from 0.40 to 0.80 in almost models, which indicate that some models have higher deviations in relation to the CCMP. The spatial correlation display values between 0.80 and 0.90; however, few RCMs have values higher than 0.90, including the two ROM simulations. The high values of S, larger than 80% and for most of models higher than 90%, indicate an overlap between the RCMs and observed wind speed PDFs by more than 80% (Figure S1 in the supporting information). Thus, the RCMs display a good performance in reproducing the near-surface wind speed distribution, what is further emphasized by the low Yule-Kendall score values. Regarding the analysis of the PDFs, most RCMs show an overestimation in the occurrence of strong wind speeds (between 8 and 20 m/s) and a general underestimation of the occurrence of daily wind speeds ranging 1 to 8 m/s (Figure S1). Concerning the evaluation of the near-surface wind speed, the ROM-coupled run exhibits one of the best performances, better than uncoupled model and most of the CORDEX-Africa individual RCMs. From this last set of simulations, the SMHI2 and KNMI2 are the two RCMs that show lower errors.

The seasonal patterns of the near-surface wind speed for the present climate are presented in Figure 2 for the CCMP data set, ROM uncoupled and coupled simulations, and CORDEX-Africa RCMs multimodel ensemble. The seasons are defined as austral summer (December–February; DJF), autumn (March–May; MAM), winter (June–August; JJA), and spring (September–November; SON), respectively. An overall view reveals

Table 2

ROM and CORDEX-Africa Individual RCMs Errors Computed Considering the CCMP Surface Wind Data Set as Reference

RCMs	Bias%	MAPE%	Normalized standard deviation	Wilmott-D	Spatial correlation	S	Yule-Kendall
0.25°							
ROM_U	11.08	12.52	1.20	0.46	0.91	86.96	0.003
ROM_C	6.15	8.37	1.21	0.64	0.93	90.76	−0.023
0.44°							
CLM1	5.77	11.53	1.50	0.50	0.85	86.87	0.024
CLM2	3.03	7.17	1.30	0.74	0.88	91.45	0.062
CLM3	5.90	11.94	1.41	0.48	0.80	84.40	0.042
CLM4	5.65	9.41	1.34	0.59	0.88	87.93	0.036
DMI	16.05	18.13	1.35	0.23	0.88	80.67	−0.051
KNMI1	−0.28	8.48	1.43	0.63	0.90	94.55	−0.045
KNMI2	1.68	5.42	1.18	0.80	0.93	98.19	−0.010
MPI1	11.81	13.84	1.37	0.40	0.90	85.64	−0.020
MPI2	10.22	11.17	1.18	0.51	0.92	88.62	0.010
SMHI1	2.64	7.08	1.21	0.68	0.87	96.97	−0.006
SMHI2	1.36	5.79	1.07	0.79	0.83	96.88	0.016
SMHI3	2.63	8.02	1.11	0.64	0.82	95.60	0.013
SMHI4	3.04	7.46	1.09	0.67	0.82	96.80	0.007
SMHI5	9.53	11.37	1.29	0.49	0.80	88.45	−0.021
SMHI6	2.77	6.01	1.13	0.73	0.85	95.68	−0.015
SMHI7	-2.44	6.48	1.01	0.71	0.83	93.83	0.003
SMHI8	3.05	6.01	0.98	0.73	0.88	95.64	0.009
SMHI9	6.14	9.28	1.22	0.59	0.85	91.25	−0.026
SMHI10	3.78	6.85	1.25	0.69	0.88	95.70	0.005
EnsFull	3.18	5.41	1.10	0.76	0.89	97.76	−0.009

Note. The metrics presented are the seasonal perceptual bias, MAPE, normalized standard deviation, Wilmott-D score, the yearly spatial correlation and daily S PDF matching score, and Yule-Kendall skewness measure.

that the seasonal patterns of the 10-m wind speed are similar, which is in agreement with the aforementioned high spatial correlation values. Near the coast, the interaction of the flow with the coastal headlands and capes is clear in both ROM runs and in the EnsFull, with increased wind speeds. This interaction is not so prominent in the CCMP data set since it has known problems near the coast due to the effect of the backscatter on land, contaminating the measurements of the wind speed in these points. The seasonality of the maximum 10-m wind speed near the coast is well related to the locations where BCLLJ occurs (Lima et al., 2019). Offshore, the synoptic wind speed pattern in the EnsFull and ROM coupled is quite similar to the CCMP, although during autumn (MAM) and winter (JJA), the coupled simulation displays higher wind speed values. In all seasons, is visible the incapability of the ROM uncoupled run to characterize the lower wind speeds associated to the presence of the St. Helen anticyclone.

Table 3 displays the error metrics of the SST comparison of both ROM runs against the NOAA SST data set for area A (Figure 1a). It should be noted that the uncoupled run is forced by the MPI-ESM SST, and this comparison gives a measure of the performance of the SST simulated by ROM against the SST simulated by the global model. Except for the MAE and the normalized standard deviation, where both simulations have very similar values, the ROM-coupled run shows lower errors in all the remaining metrics, which indicates an improved description of the regional SST pattern. The two ROM simulations display higher SSTs, with a bias of 1.89 °C in the uncoupled simulation and 0.42 °C in the coupled run. However, the uncoupled run has warmer SSTs, compared to the coupled run, which is a common feature in regional coupled models (H. Li et al., 2012, 2014). Most of the atmospheric-ocean GCMs from the Coupled Model Intercomparison Project Phase 5 have a warm bias in the Benguela System, as shown by Richter et al. (2012), which can be also found in both ROM simulations (Figure S2b). Our coupled simulation improves the representation of the SST in the Angola-Benguela frontal zone with respect to MPI-ESM (which is used to force the uncoupled simulation). The differences between ROM and NOAA in this region are about 5 °C, while MPI-ESM SST biases can reach 9 °C. The coupled system significantly reduces this warm bias relatively to the uncoupled simulation.
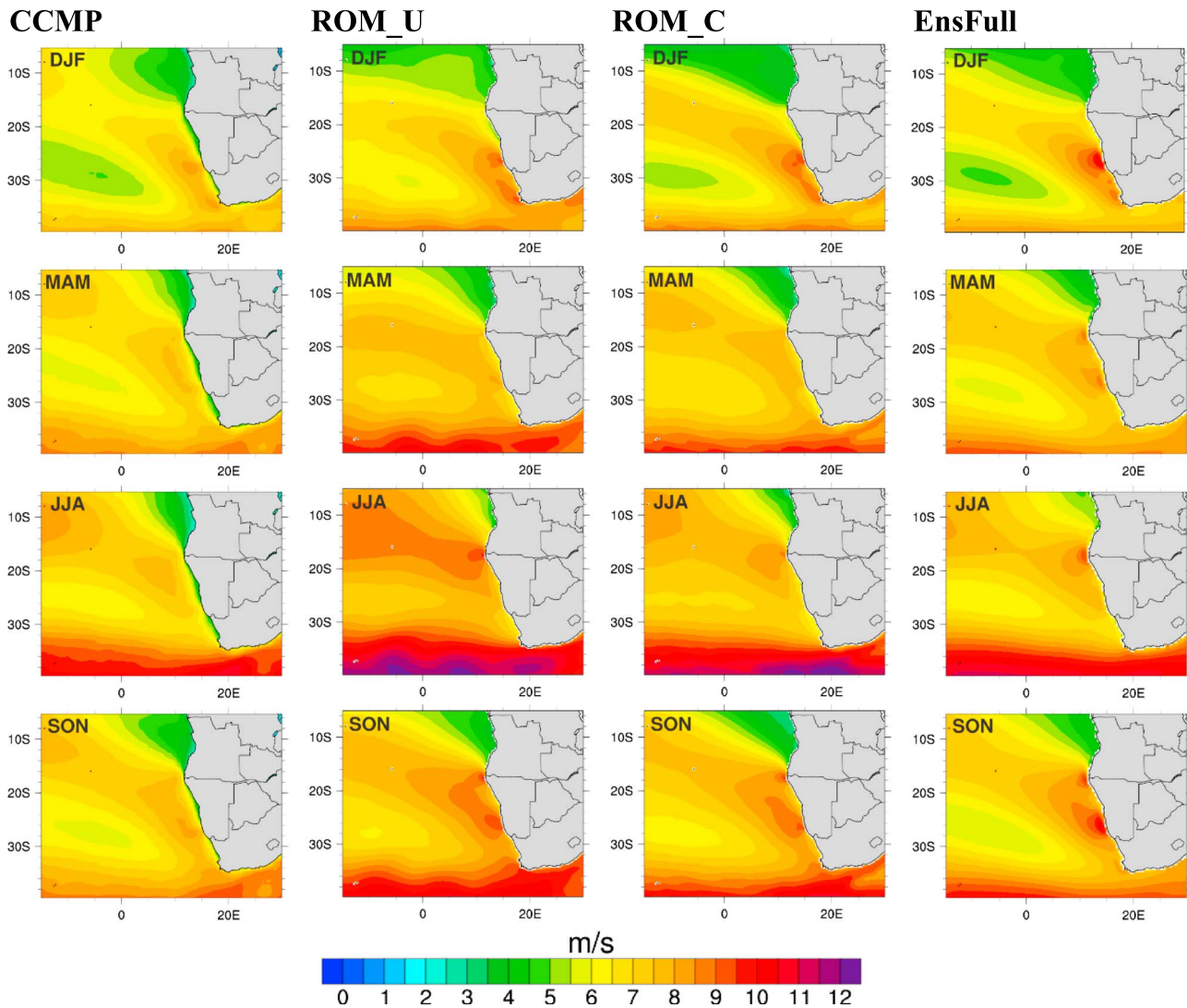
Figure 2. Seasonal mean near-surface wind speed from the CCMP observational data set (1988–2011) and from the historical ROM simulations (uncoupled and coupled) and CORDEX-Africa full multimodel ensemble (EnsFull), for 1976–2005 period.

The BCLLJ is present along the entire year, although there are two distinct positions with highest frequencies of occurrence, around 17.5°S (SON) and 26°S (DJF; Figure 3). The Benguela coastal jet has the maximum frequency of occurrence in summer (DJF), around 50% in coupled and 30% in uncoupled simulation. In MAM, the BCLLJ occurrences decreases to 15%–20% and starts to move equatorward. The BCLLJ is found at 17.5°S during winter (JJA) with frequencies of occurrence around 20% in the coupled run. In the uncoupled simulation, the occurrence is less than 10%. During spring (SON), the BCLLJ is present along the entire Namibia's offshore coast, with a mean frequency of occurrence of around 30% and a maximum located near 17.5°S.

The spatial pattern of the BCLLJ frequency of occurrence agrees well with the hindcast results presented in Lima et al. (2019), although the values are slightly lower in the historical runs. Despite the similarity between the seasonal patterns in both ROM runs, the results from ROM coupled simulation indicate a better approximation relative to the hindcast results, since the uncoupled run shows lower values of frequency of BCLLJ occurrence. The discrepancies between uncoupled hindcast and historical simulations may be related to the atmospheric forcing resolution, since the ERA-Interim (0.75°) has a higher horizontal resolution than the MPI-ESM (1.875°), but also with the differences in the large-scale forcing used in lateral

Table 3
ROM Uncoupled and Coupled SST Statistical Errors and Skill Scores Using NOAA Database as Reference

RCMs	Bias (°C)	MAE (°C)	Normalized standard deviation	Wilmott-D	Correlation	S	Yule-Kendall
ROM_U	1.89	1.95	1.13	0.60	0.87	78.05	0.053
ROM_C	0.42	1.96	1.12	0.81	0.93	87.54	0.017

Note. The metrics are the seasonal bias, MAE, normalized standard deviation and Wilmott-D, the yearly spatial correlation and daily S PDF matching score, and Yule-Kendall skewness measure.

boundary conditions (Y. Q. Wang et al., 2004). The regional climate produced by the RCMs are strongly dependent in the accuracy of the large-scale atmospheric circulation representation in reanalysis and GCM.

According to Song et al. (2009), an improvement in the SST resolution (SST gradients over ocean) can result in small-scale energy increases in the low-level wind fields. Thus, a higher resolution represents, in a detail manner, the atmospheric forcing, topographic or SST gradients over the ocean. This is particularly crucial in regions with larger SST gradients associated with ocean currents and strong ocean-atmosphere coupling, which is the case of the EBUS regions. Recent studies focused in these regions have shown that the use of regional coupled models improves the representation of mesoscale circulation and processes (Cabos et al., 2017; Desbiolles et al., 2018; H. Li et al., 2012, 2014; Renault et al., 2016; Sein et al., 2015). Also, the land-sea thermal and pressure contrasts are better captured in regional coupled models (Cabos et al., 2017; H. Li et al., 2012, 2014; Sein et al., 2015). Moreover, the improvement of the oceanic grid resolution in representing the oceanic dynamics is crucial to reduce the SST biases along the western Africa coast (Seo et al., 2006). In the present study, the ocean grid is different in the uncoupled and coupled simulations. In the uncoupled run the SST is derived directly from the MPI-ESM (~2° resolution), and in coupled simulation it is generated by the ROM model with a resolution that varies roughly from ~0.2 to ~0.5°. Therefore, the SST forcing in the coupled ROM simulation has a higher resolution than in the uncoupled one, producing more realist oceanic features, like the upwelling cold tongue (Figure S2a). The uncoupled run shows a larger coastal area with lower SSTs, while in the coupled run this area is confined to a narrow band along the coast. Consequently, the across-shore SST gradient in the coastal vicinities is better described in the coupled simulation than in the uncoupled ones. The historical seasonal pattern of the mean sea level pressure shows that
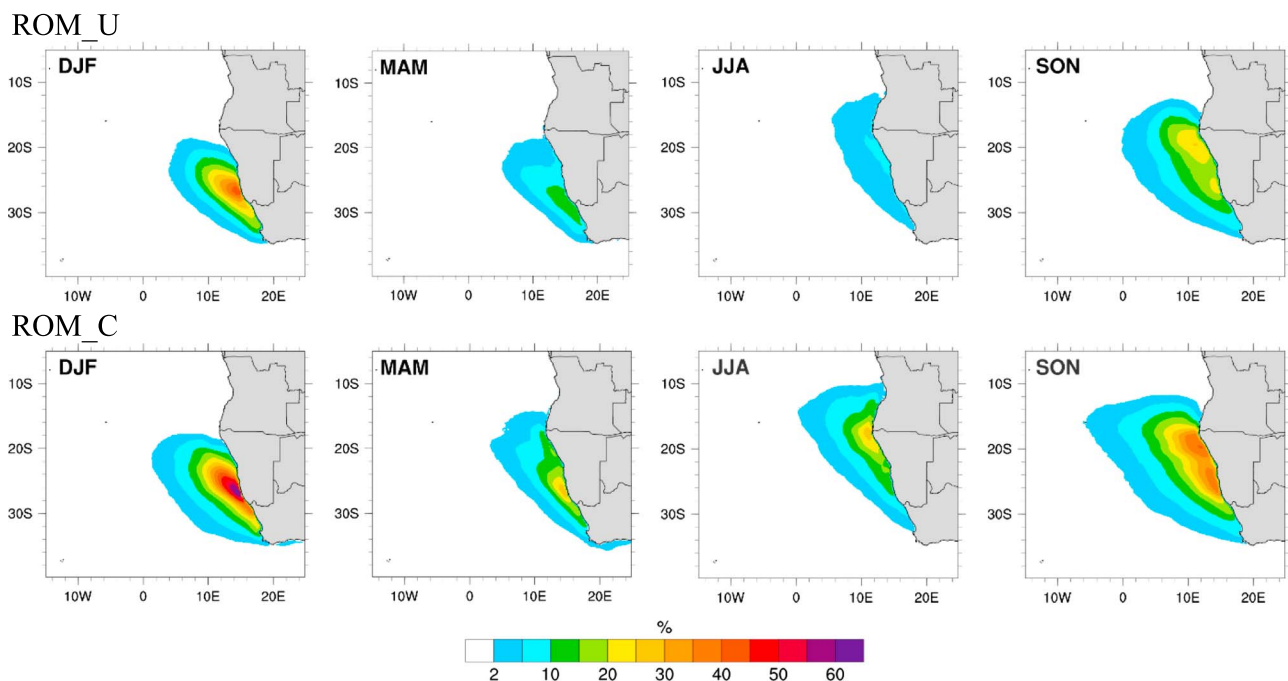

Figure 3. Seasonal maps of the BCLLJ frequency of occurrence (%) from ROM historical simulations uncoupled (top) and coupled (bottom) for all seasons (1976–2005).
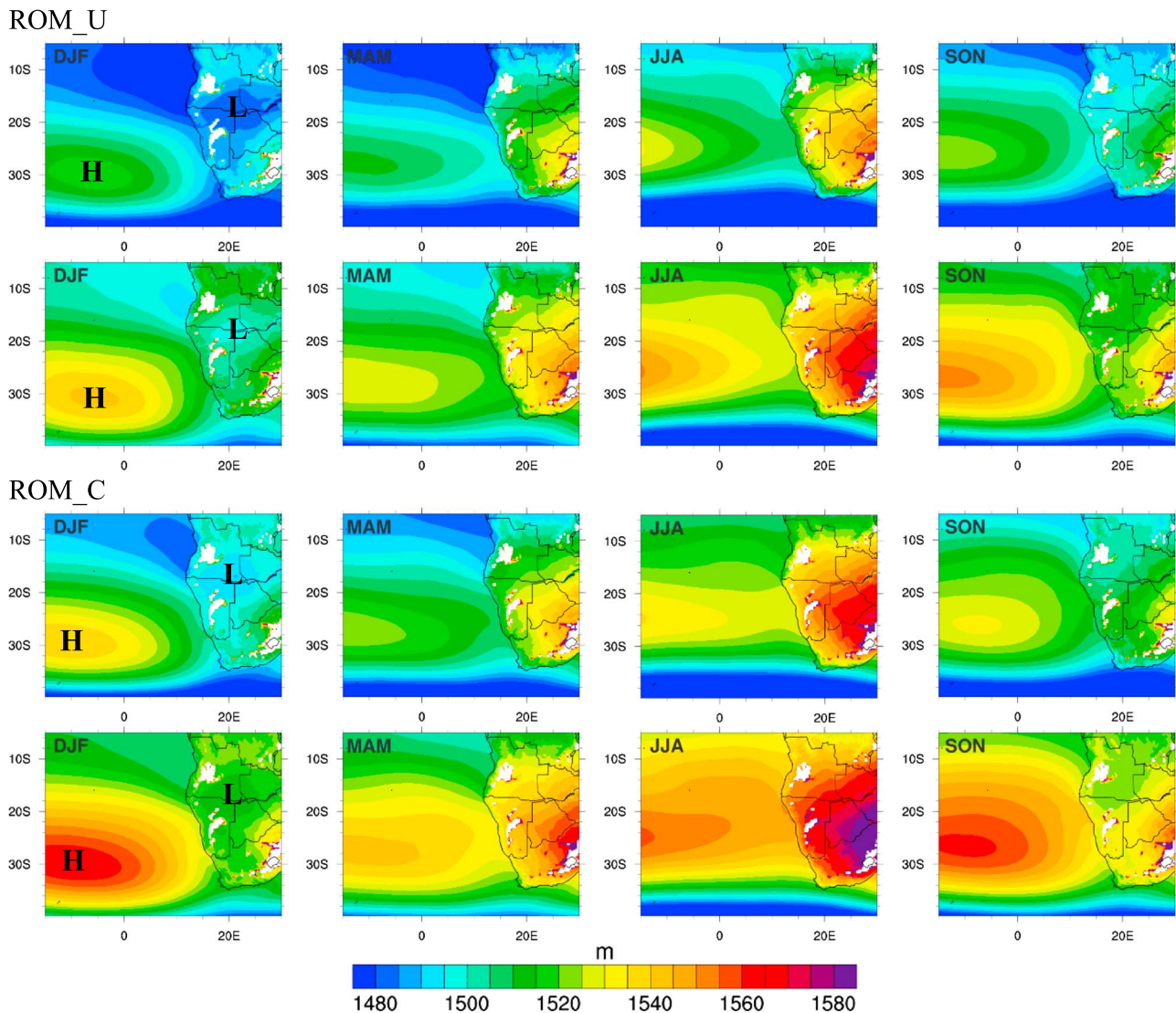
Figure 4. Seasonal mean geopotential height (m) at 850 hPa for the uncoupled (top) and coupled (bottom) ROM simulations for the historical (1976–2005) and future (2070–2099) climates. The letters **H** and **L** represent the location of the St. Helen anticyclone and the Angola thermal low, respectively.

the St. Helena anticyclone is more intense in the coupled than in the uncoupled run (Figure S3). This is in agreement with the historical 10-m wind speed pattern, where the coupled run presents lower wind speeds than in the uncoupled one (Figure 2). These differences are explained by the atmosphere-ocean interaction, where the wind speed decreases with the decrease of the SST and increases with the increase of the SST (Chelton & Xie, 2010).

4. Climate Change Impact on the Benguela CLLJ

The geopotential height at 850-hPa future projections reveal an increase of the geopotential height for both the high- and low-pressure systems over ocean and land in summer (DJF), both in the uncoupled and coupled runs (Figure 4). However, the intensification of the St. Helen anticyclone is stronger than the weakening of the Angola thermal low, leading to an increase of the land-ocean pressure gradient. In both future simulations, the projections for the end of the 21st century show an enhancement and a slight southerly displacement of the St. Helen high-pressure system, resulting in a significant positive anomaly in the cross-shore pressure gradient in all seasons, especially near the west coast of South Africa.
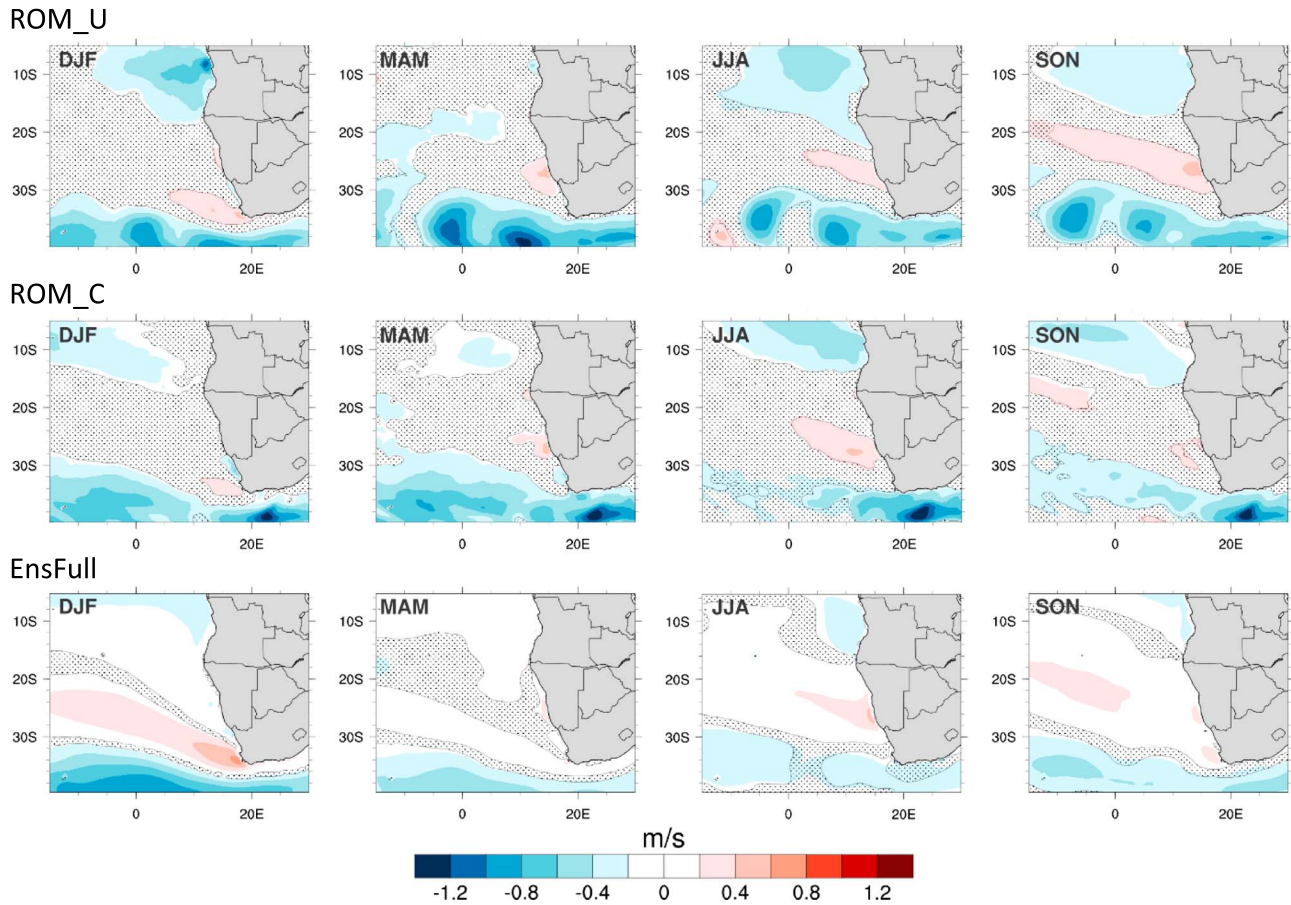
Figure 5. Seasonal mean surface wind speed anomalies, future minus present (2070–2099 minus 1976–2005), from the ROM simulations (uncoupled and coupled), and the CORDEX-Africa full multimodel ensemble. Using a Student's *t* test, the shaded areas specify changes not statistically significant at the 90% confidence level.

The projected changes of the near-surface wind speed (Figure 5) are related to the future changes of the mean sea level pressure (Figure S3). In general, the projected wind speed seasonal changes are similar between the ROM runs and the EnsFull. During summer (DJF), there is a wind speed increase in the off-shore areas of Cape Town, which is stronger in the EnsFull, and with a large meridional offshore extension. The enhancement of the flow near Cape Town (Figure 5) is a result of the increase in the pressure contrast across the southwestern coast of South Africa. In the two coastal areas, where the BCLLJ is more persistent, a slight increase in near-surface wind speed around 26°S is projected to occur in all seasons, except during summer (DJF), and a decrease in wind speed is expected north of 17.5°S. This negative signal is identified in all seasons with differences in the values, particularly in the ROM uncoupled run. An identical signal is found south of the Benguela region, where the projected decrease in 10-m wind speed is larger in the uncoupled simulation, reaching 1 m/s. This decrease of the near-surface wind speed is related to southward shift of the St. Helen anticyclone.

Since the upwelling in the Benguela region is an important regional feature and it is linked to the near-surface wind speed, the differences between future and historical climates for the cross-shore Ekman transport, $M_\perp$, were computed following equation (5) (Ekman, 1905) and are displayed in Figure S4.

$$M_\perp = \frac{\tau_\parallel}{f \cdot \rho_w} \qquad (5)$$

where $\tau_\parallel = \rho_a \cdot C_D \cdot \left| \vec{V}_{10m} \right| \cdot (\cos\phi \cdot v - \sin\phi \cdot u)$ is the along-shore wind stress, ρ_a is the air density, C_D is the drag coefficient, u and v are the wind speed components, ϕ is the angle of the coastline counterclockwise from the true north, f is the Coriolis parameter, and ρ_w is the water density.
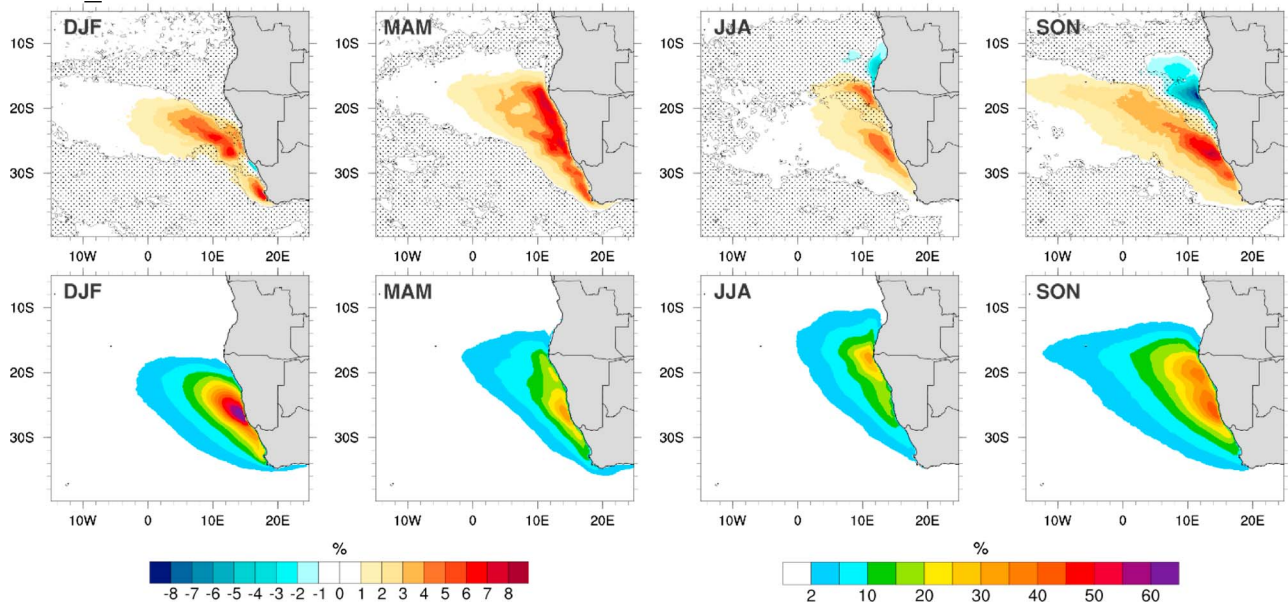
ROM_U
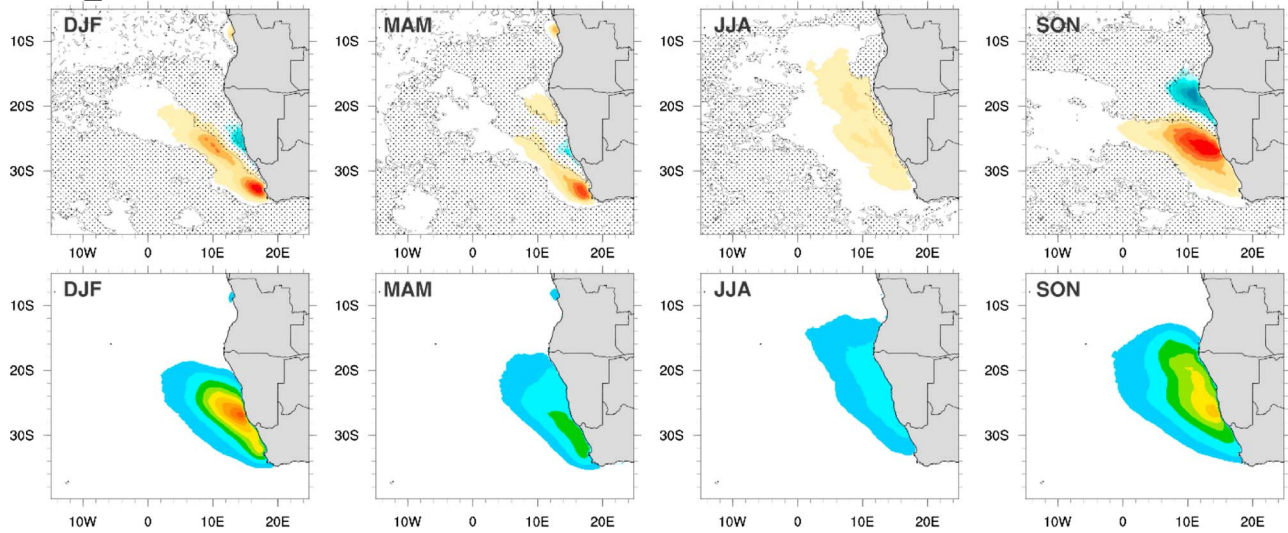
ROM_C

Figure 6. Seasonal maps of the BCLLJ frequency of occurrence (%) anomaly (2070–2099 minus 1976–2005) and future climate from ROM simulations uncoupled (top) and coupled (bottom). Using a Student's *t* test, the shaded areas specify changes not statistically significant at the 90% confidence level.

In area A2 there is a projected increase in the cross-shore Ekman transport in all seasons, in agreement with Wang et al. (2015), which have showed a positive trend in duration and intensity of the upwelling events at high latitudes in the Benguela region. This is related to the intensification of the flow, lowering the SST and enhancing the cross-shore temperature gradient. During summer (DJF) and spring (SON), in area A1, a decrease in cross-shore Ekman transport is visible and it is related to the weakening of the near-surface wind speed (Figure 5).

The intensification and southward shift of the St. Helen's high-pressure system results in a stronger pressure gradient near the west coast of South Africa. There is a projected increase in the temperature over land, due to climate warming, for all seasons, fed by to the intensive in-land radiative heating (Dosio & Panitz, 2016). The future changes of 2-m temperature on both ROM simulations are similar, although the coupled simulation displays slightly higher values over land (not shown). Regarding the projected changes for the SST field, there are noteworthy differences between the ROM uncoupled and coupled runs, particularly in the two
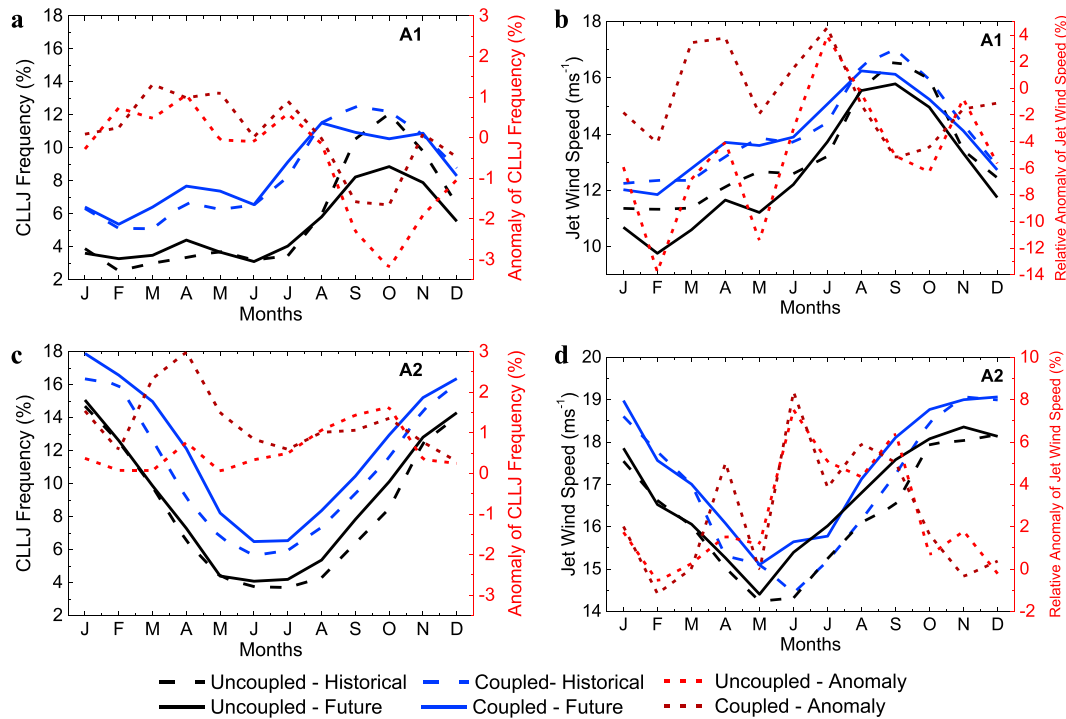
Figure 7. Intra-annual cycle (at the monthly scale) of the BCLLJ (a, c) frequency of occurrence (%) and (b, d) jet wind speed for the A1 (top) and A2 (bottom). The different areas are identified in Figure 1. The black dash and solid lines represent the uncoupled historical and future runs, respectively, and the blue dash and solid lines the coupled historical and future runs, respectively. The dash red and brown lines represent the anomaly for the uncoupled and coupled simulations, respectively.

areas where the BCLLJ occurs more persistently (Figure S5). Both simulations project warmer SSTs, with a larger heating in the uncoupled run. This simulation reveals an SST increase between 2 °C and 3.5 °C in both areas. However, it is worth noticing that area A1 presents warmer SSTs than area A2. On the other hand, the coupled simulation projects an increase in SST lesser than 1.6 °C in area A2, for all seasons, and higher than 3 °C in area A1, especially in spring (SON) season.

The expected changes for the frequency of occurrence of the BCLLJ are stronger in the coupled than in the uncoupled run (Figure 6). Since the results from the coupled run are closer to the ones from the hindcast run (Lima et al., 2019), future projections from this simulation may be expected to be a closer representation of the climate at the end of the 21st century.

The ROM-coupled run shows an increase in the BCLLJ frequency of occurrence around the southern area in all seasons, extending along the coast but also further offshore of the west coast of Namibia. In summer (DJF), an increase of around 6% in the BCLLJ is expected, as well as an offshore expansion of the coastal jet occurrences in southern area. Along the entire west Namibia coast there is an increase of about 7%, which enhances the frequency of occurrence to ~25% during the autumn (MAM) season. In winter (JJA), the signal is identical to autumn (MAM) but with lower projected changes. During spring (SON), there is dipole between the northern and southern areas. In the northern area, a reduction of about 8% is projected according to coupled simulation.

The uncoupled run displays similar spatial patterns of projected changes compared to the coupled run, although the signal is less strong and the offshore extension of the BCLLJ is less pronounced. The same dipole between north and south areas is projected for the spring (SON) season, with a reduction and an increase of around 6%, respectively. During summer (DJF) and autumn (MAM) seasons, there is a slight decrease of about 3% around 26°S.

The intra-annual cycle (at the monthly scale) of the BCLLJ frequency of occurrence and jet wind speed show significant changes between the historical and the projected future climates in both ROM simulations (Figure 7). The monthly anomalies (future minus historical) of these two variables are rather different for
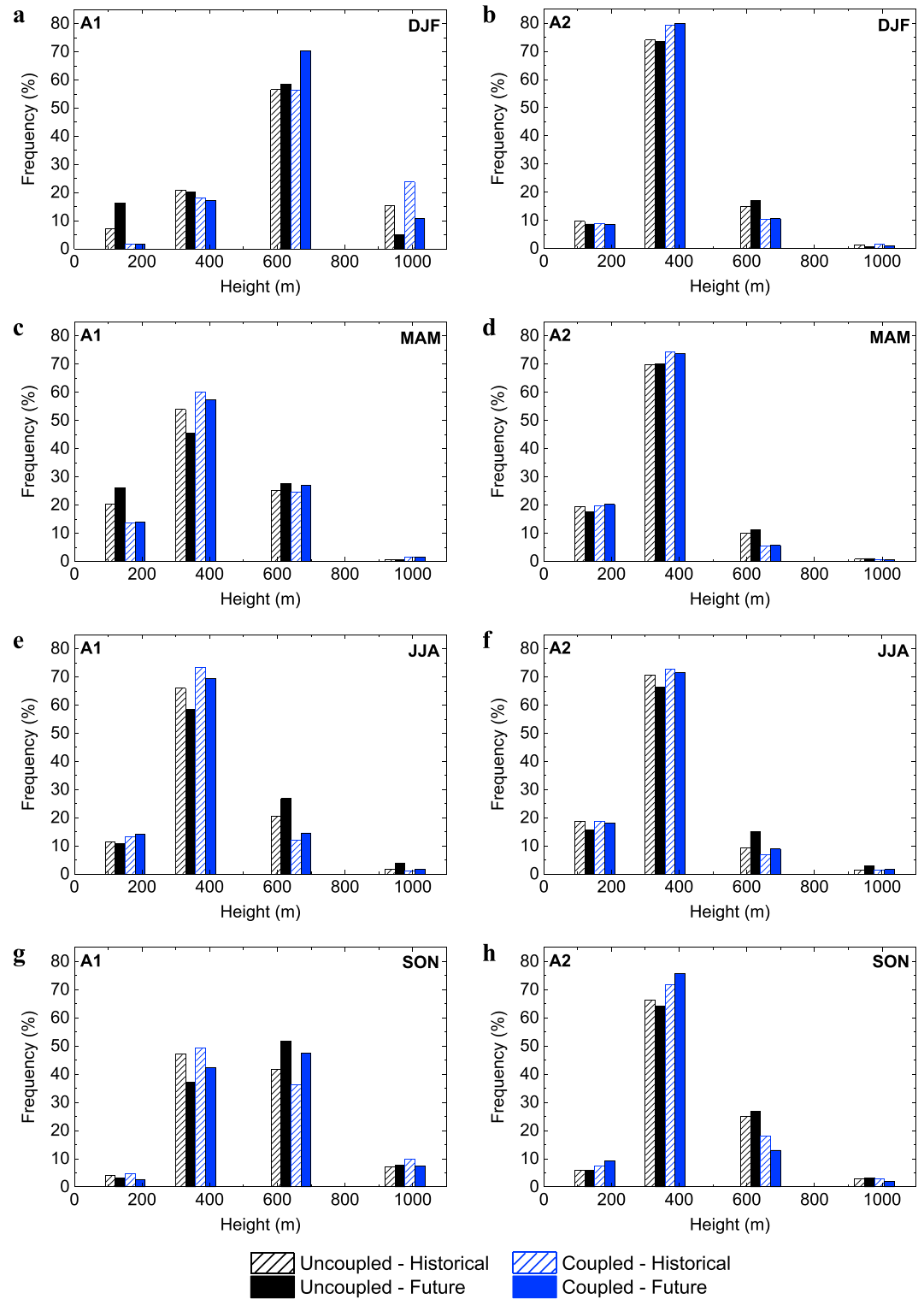
Figure 8. Histograms of jet height for area A1 (left) and A2 (right) for all seasons: (a, b) DJF, (c, d) MAM, (e, f) JJA, and (g, h) SON.

the two regions. For the BCLLJ frequency of occurrence, in A1, there is a clear decrease from August to November, higher in the uncoupled simulation (around −3% in October). In the remaining months, there is a slight increase (lower than 1%) in the two ROM runs. In A2, the signal of the frequency of occurrence
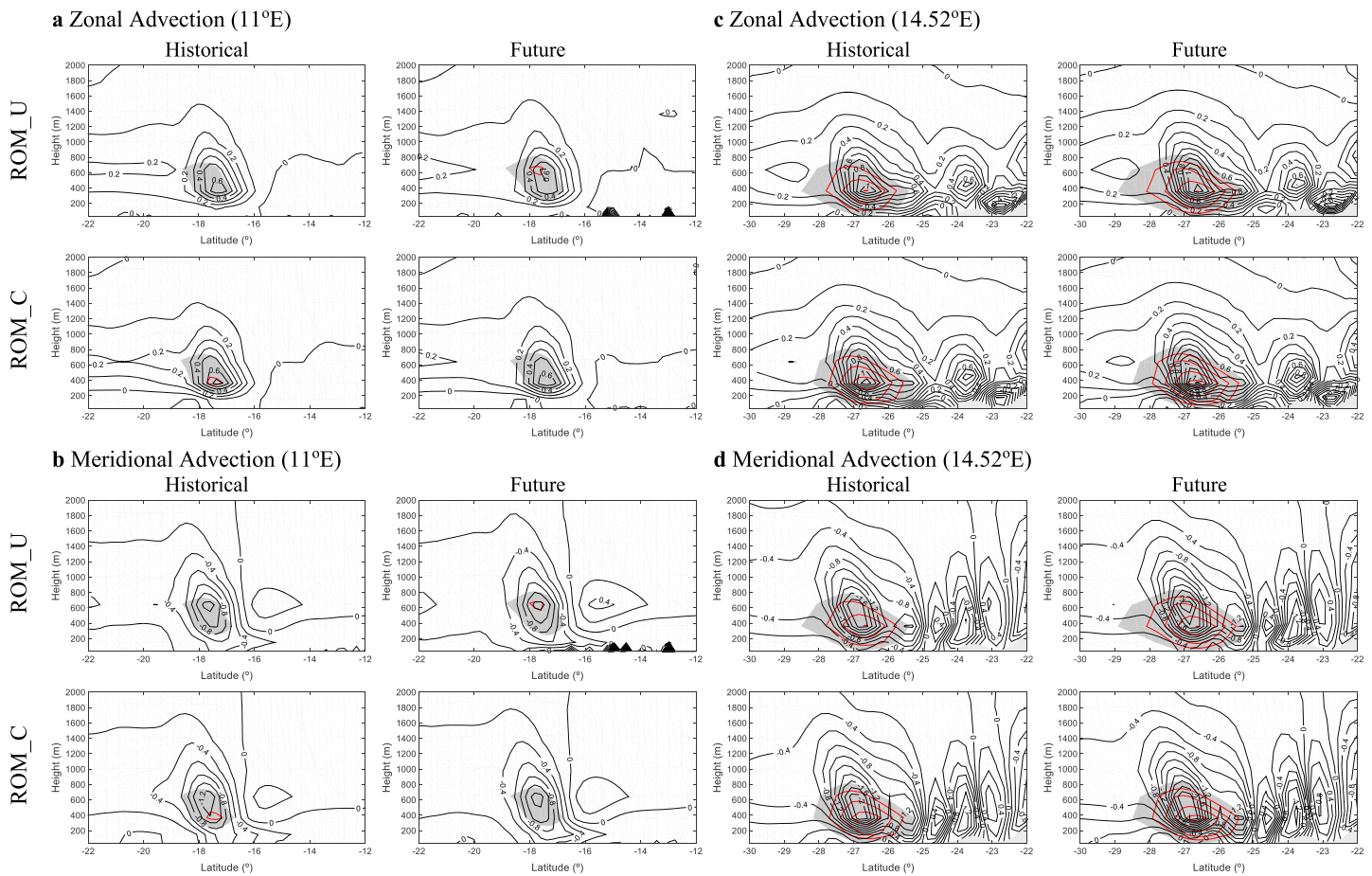
Figure 9. Along section at 11°E and 14.52°E during spring (SON) of (a, c) zonal advection and (b, d) meridional advection (K/hr; black lines) of the liquid water potential temperature budget for ROM uncoupled and coupled historical and future simulations, when jet occurs. The shading grey regions correspond to winds higher than 14 m/s, with contour interval of 1 m/s (red line).

is different, as observed in the seasonal cycle (Figure 6). Both ROM simulations reveal an increase in the BCLLJ frequency of occurrence in all months, although for the autumn (MAM) months, the coupled simulation displays larger anomalies than the uncoupled one (around 2%). Regarding the BCLLJ wind speed, the projected changes are more pronounced. In A1, from July to November, the changes are similar between the ROM simulations. There is a slight increase in July around 4% and a decrease in the remaining months. From December to June, the uncoupled run projected a significant decrease in the jet wind speed, more noticeable in February and May (around −13% and −11%, respectively). The coupled simulation shows an oscillation between −4% to 4% from January to June. The future changes for A2 are quite consistent between uncoupled and coupled runs. There is an increase in the BCLLJ wind speed for all months, more significant from June to September (between 4% and 8%).

The future projections regarding the jet height are presented in Figure 8, for both ROM simulations and for all seasons. The A1 shows higher differences between future and present climates than A2. In the latter, the most prevalent height of jet occurrence is around 360 m (>65%); however, there is a slight increase of the jet occurrence at higher altitudes lesser than 5%, in all seasons. In A1, there is a shift for higher altitudes in all seasons, although during summer (DJF), a decrease of the jet occurrences is found around 980 m.

To analyze the changes in the land-sea thermal contrast, the zonal and meridional advective terms of the liquid water potential temperature budget are computed. The liquid water potential temperature is computed accordingly to equation (6) (Deardorff, 1976) and the related budget with equation (7) (Stull, 1988).

$$\theta_L = \theta - \frac{\theta}{T}\frac{L}{c_p}q_c \tag{6}$$

where T is the temperature, θ is the potential temperature, L is the latent heat of vaporization, c_p is the specific heat at constant pressure, and q_c is the liquid water content.

$$\frac{\partial \theta_L}{\partial t} = -U\frac{\partial \theta_L}{\partial x} - V\frac{\partial \theta_L}{\partial y} - W\frac{\partial \theta_L}{\partial z} + \theta_{L'r} + \theta_{L'm} \tag{7}$$

where the terms (left to right) represent the local time change, zonal, meridional and vertical advection, radiative tendency, and mixing. The zonal and meridional advective terms were computed using the second-order central-difference approximation.

Since the spring (SON) season shows a decrease and an increase of the BCLLJ frequency of occurrence in northern (A1) and southern (A2) areas, Figure 9 displays the along section of the zonal and meridional liquid water potential temperature advection at 11°E and 14.52°E for historical and future climates for this season.

The zonal advection term in the θ_L budget shows maximum heating rates at and above the jet core, which implies advection of continental warm air to the ocean (Figures 9a and 9c). The meridional advection term is responsible for the advection of cooler air at and south of the jet core and advection of warmer air to the north (Figures 9b and 9d). The coupled simulation shows higher values in these two terms, which means that the thermal contrast between land and ocean is higher when compared with uncoupled run. In area A1 (Figures 9a and 9b), the future projection displays a decrease in the zonal advection of warm air from the continent and meridional advection of cooler air from south of the jet core, revealing a decrease in thermal contrast between land and ocean, an important feature for the coastal jet occurrence. This decrease is higher in coupled run than in uncoupled, meaning that the reduction in land-ocean thermal gradient is higher in the former. Also, a slight decline of the wind speed at jet core is presented in coupled run.

In area A2 (Figures 9c and 9d), the future projections of the zonal and meridional advective terms in θ_L budget show opposite signals, compared to the area A1. The zonal term reveals an increase in advection of continental warm air (Figure 9c), and the meridional term displays also an increase of advection of cooler air from south of the jet core (Figure 9d). The projected changes have a similar result between both simulations; however, the coupled simulations show slightly higher values in the advective terms. At the jet core, the BCLLJ is projected to intensify.

5. Discussion and Conclusions

The main objective of the current study was to understand how the BCLLJ may change with the impact of the climate change, toward the end of the 21st century. The projected changes of the spatial and temporal variability of the BCLLJ frequency of occurrence and wind speed were investigated. The study of the climate change impact was done using two ROM simulations (uncoupled and coupled mode) at 25-km horizontal resolution, for two different periods: 1976–2005 and 2070–2099 following the RCP8.5 greenhouse gases emissions scenario. The expected changes of the synoptic forcing and land-sea thermal contrasts were also analyzed. The future pattern of near-surface wind speed was also assessed, with the support of the CORDEX-Africa multimodel ensemble.

The evaluation of the near-surface wind speed from ROM uncoupled and coupled runs and CORDEX-Africa individual RCMs and multimodel ensemble, against the CCMP observational data set, showed that the ROM-coupled simulation displayed the best performance in representing the surface wind features. The ROM-coupled simulation revealed an improvement of the known warm bias of SST in the Benguela upwelling system. Also, the results of BCLLJ frequency of occurrence from historical coupled simulation presented a better approximation of the hindcast results compared with uncoupled run, although with lower values of BCLLJ frequency of occurrence.

The reported changes in land-sea thermal and pressure contrasts largely explain the projected changes in the future BCLLJ frequency of occurrence and wind speed in the southern area (A2). Offshore west South Africa, a slight strengthening of the flow is a result of the southerly displacement and the intensification of the St. Helen's anticyclone, resulting in lower changes of SST over this region (Figure S5). However, a north-south

latitudinal increase of the SST is expected to occur in a future climate, higher in the uncoupled than in coupled run, mainly in the southern area. The increase of the coastal parallel wind speeds over the ocean generates an increase in upwelling currents due to the offshore Ekman transport, bringing deep cold water to the surface, which in turn results in a decrease of the SST, attenuating the global warming effects on the SST. Consequently, the land-ocean thermal contrast intensifies due to the higher temperatures over land. An increase in advection of warmer air from the continent and cooler air from the south of the jet core is projected to occur. The strengthening of the thermal and pressure gradients are in agreement with stronger baroclinicity, which leads to the occurrence of the BCLLJ (Burk & Thompson, 1996), resulting in a thermal wind structure that increase the BCLLJ wind speed. Consequently, offshore South Africa, an increase in the BCLLJ frequency of occurrence during summer (DJF) and autumn (MAM) seasons, in both ROM simulations, is projected to occur. However, around 26°S this increase is present in all seasons on the coupled run. On the other hand, the BCLLJ wind speed projections show a year-round intensification for both simulations. Results concerning the increase in BCLLJ occurrence are in agreement with the upwelling projections, which show, for the Benguela region, a strengthening at high latitudes (25–35°S), with high correlation with the land-sea thermal contrasts (Bakun, 1990; D. Wang et al., 2015). Hence, a reinforcement in the positive feedback between the BCLLJ occurrence and upwelling events is expected in the southern area of BCLLJ occurrence.

Conversely, in the northern area (A1), the projected pressure gradient has no noticeable changes, but there is a projected decrease in the thermal contrast due to the warmer SST, particularly during spring (SON). This results in a decrease in advection of warmer air from land and cooler air from south of the jet core. Furthermore, this season presents a larger decrease of the wind speed at jet height in the uncoupled run when compared to the coupled run. This can be explained since the former presents a higher increase of SST than the latter. The decrease of the coast-parallel winds over the ocean generates less upwelling currents due to the offshore Ekman transport, bringing less deep cold water to the surface, which results in an increase of the SST. In this area, the projections reveal a negative feedback between upwelling and BCLLJ occurrence; that is, an SST increase leads to a decrease in the wind speed along the coast, which results in a reduction of the upwelling events and subsequently to a projected decrease in the BCLLJ frequency of occurrence.

In summary, the increase of the BCLLJ frequency of occurrence and the upwelling enhance the feedback between these two regional features toward the end of the 21st century in southern area, leading to an intensification of the BCLLJ. In contrast, during spring (SON) in northern area, a negative feedback was projected since there is a decrease and weakening of the BCLLJ events. The current study was the first one using coupled and uncoupled high resolution to address the climate change impact on the BCLLJ system. The extension of this work to investigate the impact of the changes of the BCLLJ on the regional climate, improving the understanding about the enhancement of the key feedbacks between BCLLJ, upwelling, and aridity, is projected for a near future using the coupled ROM simulation.

References

Atlas, R., Hoffman, R. N., Ardizzone, J., Leidner, S. M., Jusem, J. C., Smith, D. K., & Gombos, D. (2011). A cross-calibrated, multiplatform ocean surface wind velocity product for meteorological and oceanographic applications. *Bulletin of the American Meteorological Society*, *92*(2), 157–174. https://doi.org/10.1175/2010BAMS2946.1

Bakun, A. (1990). Global climate change and intensification of coastal ocean upwelling. *Science*, *247*(4939), 198–201. https://doi.org/10.1126/science.247.4939.198

Bakun, A., Black, B. A., Bograd, S. J., García-Reyes, M., Miller, A. J., Rykaczewski, R. R., & Sydeman, W. J. (2015). Anticipated effects of climate change on coastal upwelling ecosystems. *Current Climate Change Reports*, *1*(2), 85–93. https://doi.org/10.1007/s40641-015-0008-4

Beardsley, R. C., Dorman, C. E., Friehe, C. A., Rosenfeld, L. K., & Winant, C. D. (1987). Local atmospheric forcing during the Coastal Ocean Dynamics Experiment: 1. A description of the marine boundary layer and atmospheric conditions over a northern California upwelling region. *Journal of Geophysical Research*, *92*(C2), 1467–1488. https://doi.org/10.1029/JC092iC02p01467

Burk, S. D., & Thompson, W. T. (1996). The summertime low-level jet and marine boundary layer structure along the California coast. *Monthly Weather Review*, *124*(4), 668–686. https://doi.org/10.1175/1520-0493(1996)124<0668:TSLLJA>2.0.CO;2

Cabos, W., Sein, D. V., Pinto, J. G., Fink, A. H., Koldunov, N. V., Alvarez, F., et al. (2017). The South Atlantic Anticyclone as a key player for the representation of the tropical Atlantic climate in coupled climate models. *Climate Dynamics*, *48*(11–12), 4051–4069. https://doi.org/10.1007/s00382-016-3319-9

Cardoso, R. M., Soares, P. M. M., Lima, D. C. A., & Miranda, P. M. A. (2018). Mean and extreme temperatures in a warming climate: EURO CORDEX and WRF regional climate high-resolution projections for Portugal. *Climate Dynamics*, *52*(1-2), 129–157. https://doi.org/10.1007/s00382-018-4124-4

Cardoso, R. M., Soares, P. M. M., Lima, D. C. A., & Semedo, A. (2016). The impact of climate change on the Iberian low-level wind jet: EURO-CORDEX regional climate simulation. *Tellus, Series A: Dynamic Meteorology and Oceanography*, *68*, 1–15. https://doi.org/10.3402/tellusa.v68.29005

Chelton, D., & Xie, S.-P. (2010). Coupled ocean-atmosphere interaction at oceanic mesoscales. *Oceanography*, *23*(4), 52–69. https://doi.org/10.5670/oceanog.2010.05

Christensen, J. H., Kjellström, E., Giorgi, F., Lenderink, G., & Rummukainen, M. (2010). Weight assignment in regional climate models. *Climate Research*, *44*(2–3), 179–194. https://doi.org/10.3354/cr00916

Christensen, O. B., Drews, M., Christensen, J. H., Dethloff, K., Ketelsen, K., Hebestadt, I., & Rinke, A. (2007). The HIRHAM Regional Climate Model Version 5 (beta). Technical Report 06-17;, 1–22.

Deardorff, J. W. (1976). Usefulness of liquid-water potential temperature in a shallow-cloud model. *Journal of Applied Meteorology*, *15*(1), 98–102. https://doi.org/10.1175/1520-0450(1976)015<0098:UOLWPT>2.0.CO;2

Desbiolles, F., Blamey, R., Illig, S., James, R., Barimalala, R., Renault, L., & Reason, C. (2018). Upscaling impact of wind/sea surface temperature mesoscale interactions on southern Africa austral summer climate. *International Journal of Climatology*, *38*(12), 4651–4660. https://doi.org/10.1002/joc.5726

Dosio, A., & Panitz, H. J. (2016). Climate change projections for CORDEX-Africa with COSMO-CLM regional climate model and differences with the driving global climate models. *Climate Dynamics*, *46*(5–6), 1599–1625. https://doi.org/10.1007/s00382-015-2664-4

Ekman, V. W. (1905). On the influence of the Earth's rotation on ocean-currents. *Arkiv foer Matematik, Astronomi, och Fysik*, *2*(11), 1–52.

Ferro, C. A. T., Hannachi, A., & Stephenson, D. B. (2005). Simple nonparametric techniques for exploring changing probability distributions of weather. *Journal of Climate*, *18*(21), 4344–4354. https://doi.org/10.1175/JCLI3518.1

Fréon, P., Arístegui, J., Bertrand, A., Crawford, R. J. M., Field, J. C., Gibbons, M. J., et al. (2009). Functional group biodiversity in Eastern Boundary Upwelling Ecosystems questions the wasp-waist trophic structure. *Progress in Oceanography*, *83*(1–4), 97–106. https://doi.org/10.1016/j.pocean.2009.07.034

Giorgetta, M. A., Jungclaus, J., Reick, C. H., Legutke, S., Bader, J., Böttinger, M., et al. (2013). Climate and carbon cycle changes from 1850 to 2100 in MPI-ESM simulations for the Coupled Model Intercomparison Project Phase 5. *Journal of Advances in Modeling Earth Systems*, *5*, 572–597. https://doi.org/10.1002/jame.20038

Giorgi, F., Jones, C., & Asrar, G. R. (2009). Addressing climate information needs at the regional level: The CORDEX framework. *WMO Bulletin*, *58*(November 2008), 175–183.

Intergovernmental Panel on Climate Change (2014). Climate Change 2013: The Physical Science Basis. In *Contribution of Working Group I to the Fifth Assessment Report of the Intergovernmental Panel on Climate Change. the Fifth Assessment Report* (Vol. 5, 1535 pp.). Cambridge: Cambridge University Press.

Jacob, D., Van Den Hurk, B. J. J. M., Andræ, U., Elgered, G., Fortelius, C., Graham, L. P., et al. (2001). A comprehensive model intercomparison study investigating the water budget during the BALTEX-PIDCAP period. *Meteorology and Atmospheric Physics*, *77*(1–4), 19–43. https://doi.org/10.1007/s007030170015

Li, D., von Storch, H., Yin, B., Xu, Z., Qi, J., Wei, W., & Guo, D. (2018). Low-level jets over the Bohai Sea and Yellow Sea: Climatology, variability, and the relationship with regional atmospheric circulations. *Journal of Geophysical Research: Atmospheres*, *123*, 5240–5260. https://doi.org/10.1029/2017JD027949

Li, H., Kanamitsu, M., & Hong, S. Y. (2012). California reanalysis downscaling at 10 km using an ocean-atmosphere coupled regional model system. *Journal of Geophysical Research*, *117*, D12118. https://doi.org/10.1029/2011JD017372

Li, H., Kanamitsu, M., Hong, S. Y., Yoshimura, K., Cayan, D. R., & Misra, V. (2014). A high-resolution ocean-atmosphere coupled downscaling of the present climate over California. *Climate Dynamics*, *42*(3–4), 701–714. https://doi.org/10.1007/s00382-013-1670-7

Lima, D. C. A., Soares, P. M. M., Semedo, A., & Cardoso, R. M. (2018). A Global View of Coastal Low-Level Wind Jets Using an Ensemble of Reanalyses. *Journal of Climate*, *31*(4), 1525–1546. https://doi.org/10.1175/JCLI-D-17-0395.1

Lima, D. C. A., Soares, P. M. M., Semedo, Á., Cabos, W., & Sein, D. V. (2019). A Climatological Analysis of the Benguela Coastal Low-Level Jet. *Journal of Geophysical Research: Atmospheres*, *124*. https://doi.org/10.1029/2018JD028944

Nicholson, S. E. (2010). A low-level jet along the Benguela coast, an integral part of the Benguela current ecosystem. *Climatic Change*, *99*(3), 613–624. https://doi.org/10.1007/s10584-009-9678-z

Parish, T. R. (2000). Forcing of the Summertime Low-Level Jet along the California Coast. *Journal of Applied Meteorology*, *39*(12), 2421–2433. https://doi.org/10.1175/1520-0450(2000)039<2421:FOTSLL>2.0.CO;2

Perkins, S. E., Pitman, A. J., Holbrook, N. J., & McAneney, J. (2007). Evaluation of the AR4 climate models' simulated daily maximum temperature, minimum temperature, and precipitation over Australia using probability density functions. *Journal of Climate*, *20*(17), 4356–4376. https://doi.org/10.1175/JCLI4253.1

Ranjha, R., Svensson, G., Tjernström, M., & Semedo, A. (2013). Global distribution and seasonal variability of coastal low-level jets derived from ERA-Interim reanalysis. *Tellus A: Dynamic Meteorology and Oceanography*, *65*, 1–21. https://doi.org/10.3402/tellusa.v65i0.20412

Ranjha, R., Tjernström, M., Semedo, A., Svensson, G., & Cardoso, R. M. (2015). Structure and variability of the Oman coastal low-level jet. *Tellus, Series A: Dynamic Meteorology and Oceanography*, *67*(1), 1–20. https://doi.org/10.3402/tellusa.v67.25285

Renault, L., Molemaker, M. J., McWilliams, J. C., Shchepetkin, A. F., Lemarié, F., Chelton, D., et al. (2016). Modulation of wind work by oceanic current interaction with the atmosphere. *Journal of Physical Oceanography*, *46*(6), 1685–1704. https://doi.org/10.1175/JPO-D-15-0232.1

Reynolds, R. W., Smith, T. M., Liu, C., Chelton, D. B., Casey, K. S., & Schlax, M. G. (2007). Daily high-resolution-blended analyses for sea surface temperature. *Journal of Climate*, *20*(22), 5473–5496. https://doi.org/10.1175/2007JCLI1824.1

Riahi, K., Rao, S., Krey, V., Cho, C., Chirkov, V., Fischer, G., et al. (2011). RCP 8.5—A scenario of comparatively high greenhouse gas emissions. *Climatic Change*, *109*(1–2), 33–57. https://doi.org/10.1007/s10584-011-0149-y

Richter, I., Xie, S. P., Wittenberg, A. T., & Masumoto, Y. (2012). Tropical Atlantic biases and their relation to surface wind stress and terrestrial precipitation. *Climate Dynamics*, *38*(5–6), 985–1001. https://doi.org/10.1007/s00382-011-1038-9

Rockel, B., Will, A., & Hense, A. (2008, August 25). The regional climate model COSMO-CLM (CCLM). *Meteorologische Zeitschrift*, *17*(4), 347–348. https://doi.org/10.1127/0941-2948/2008/0309

Samuelsson, P., Jones, C. G., Willén, U., Ullerstig, A., Gollvik, S., Hansson, U., et al. (2011). The Rossby Centre Regional Climate model RCA3: Model description and performance. *Tellus, Series A: Dynamic Meteorology and Oceanography*, *63*(1), 4–23. https://doi.org/10.1111/j.1600-0870.2010.00478.x

Sein, D. V., Mikolajewicz, U., Gröger, M., Fast, I., Cabos, W., Pinto, J. G., et al. (2015). Regionally coupled atmosphere-ocean-sea ice-marine biogeochemistry model ROM: 1. Description and validation. *Journal of Advances in Modeling Earth Systems*, *7*, 268–304. https://doi.org/10.1002/2014MS000357

Semedo, A., Soares, P. M. M., Lima, D. C. A., Cardoso, R. M., Bernardino, M., & Miranda, P. M. A. (2016). The impact of climate change on the global coastal low-level wind jets: EC-EARTH simulations. *Global and Planetary Change*, *137*, 88–106. https://doi.org/10.1016/j.gloplacha.2015.12.012

Seo, H., Jochum, M., Murtugudde, R., & Miller, A. J. (2006). Effect of ocean mesoscale variability on the mean state of tropical Atlantic climate. *Geophysical Research Letters*, *33*, L09606. https://doi.org/10.1029/2005GL025651

Soares, P. M. M., Cardoso, R. M., Lima, D. C. A., & Miranda, P. M. A. (2017). Future precipitation in Portugal: High-resolution projections using WRF model and EURO-CORDEX multi-model ensembles. *Climate Dynamics*, *49*(7–8), 2503–2530. https://doi.org/10.1007/s00382-016-3455-2

Soares, P. M. M., Lima, D. C. A., Cardoso, R. M., & Semedo, A. (2017). High resolution projections for the western Iberian coastal low level jet in a changing climate. *Climate Dynamics*, *49*(5–6), 1547–1566. https://doi.org/10.1007/s00382-016-3397-8

Soares, P. M. M., Lima, D. C. A., Semedo, A., Cardoso, R. M., Cabos, W., & Sein, D. V. (2018). Assessing the climate change impact on the North African offshore surface wind and coastal low-level jet using coupled and uncoupled regional climate simulations. *Climate Dynamics*, 1–22. https://doi.org/10.1007/s00382-018-4565-9

Song, Q., Chelton, D. B., Esbensen, S. K., Thum, N., & O'Neill, L. W. (2009). Coupling between sea surface temperature and low-level winds in mesoscale numerical models. *Journal of Climate*, *22*(1), 146–164. https://doi.org/10.1175/2008JCLI2488.1

Stull, R. B. (1988). *An Introduction to Boundary Layer Meteorology*. Dordrecht: Springer. https://doi.org/10.1007/978-94-009-3027-8

Sydeman, W. J., García-Reyes, M., Schoeman, D. S., Rykaczewski, R. R., Thompson, S. A., Black, B. A., & Bograd, S. J. (2014). Climate change and wind intensification in coastal upwelling ecosystems. *Science*, *345*(6192), 77–80. https://doi.org/10.1126/science.1251635

Van Meijgaard, E., Van Ulft, L. H., Van De Berg, W. J., Bosveld, F. C., Van Den Hurk, B. J. J. M., Lenderink, G., & Siebesma, A. P. (2008). The KNMI regional atmospheric climate model RACMO version 2.1.

Wang, D., Gouhier, T. C., Menge, B. A., & Ganguly, A. R. (2015). Intensification and spatial homogenization of coastal upwelling under climate change. *Nature*, *518*(7539), 390–394. https://doi.org/10.1038/nature14235

Wang, Y. Q., Leung, L. R., McGregor, J. L., Lee, D.-K. K., Wang, W.-C. C., Ding, Y. H., & Kimura, F. (2004). Regional climate modeling: Progress, challenges, and prospects. *Journal of the Meteorological Society of Japan*, *82*(6), 1599–1628. https://doi.org/10.2151/jmsj.82.1599

Wilks, D. S. (2006). Statistical Methods in the Atmospheric Sciences. In *Methods* (676 pp.). Oxford, UK: Academic Press.

Willmott, C. J., Robeson, S. M., & Matsuura, K. (2012). A refined index of model performance. *International Journal of Climatology*, *32*(13), 2088–2094. https://doi.org/10.1002/joc.2419

Winant, C. D., Dorman, C. E., Friehe, C. A., & Beardsley, R. C. (1988). The marine layer off Northern California: An example of super-critical channel flow. *Journal Of The Atmospheric Sciences*, *45*(23), 3588–3605. https://doi.org/10.1175/1520-0469(1988)045<3588:TMLONC>2.0.CO;2

Zemba, J., & Friehe, C. A. (1987). The marine atmospheric boundary layer jet in the Coastal Ocean Dynamics Experiment. *Journal of Geophysical Research*, *92*(C2), 1489. https://doi.org/10.1029/JC092iC02p01489